Journal of Ship Research, Vol. 65, No. 2, June 2021, pp. 139–152
http://dx.doi.org/10.5957/JOSR.09180083

CFD Simulations of Self-Propulsion and Turning Circle Maneuver up to 90° of Ship in Waves

Cong Liu, Jianhua Wang, and **Decheng Wan**

Computational Marine Hydrodynamics Lab (CMHL), State Key Laboratory of Ocean Engineering, School of Naval Architecture, Ocean and Civil Engineering, Shanghai Jiao Tong University, Shanghai, China

In the present work, a Reynolds-Averaged Navier-Stokes (RANS)-overset method is used to numerically investigate self-propulsion and turning circle maneuver in waves for a container ship. A computational fluid dynamics (CFD) solver naoe-FOAM-SJTU is used for the numerical computations of the fully appended Duisburg Test Case ship model. Overset grids are used to handle the motions of the ship hull appended with the propeller and the rudder. Open source toolbox waves2Foam is used to prevent wave reflection in the computational domain. The current numerical method is validated by comparing the ship speed in the self-propulsion case between CFD and Experimental Fluid Dynamics (EFD). Predicted ship 6-DOF motions, hydrodynamic forces, free surfaces, and inflow of the propeller are presented. The propulsion characteristic is mainly studied. Assuming the thrust identification method works even in unsteady conditions, the wake fraction and propulsion efficiency are discussed. The effect of orbital motion of water particle and ship motion on the propulsion performance are identified. In conclusion, the present RANS-overset method is a reliable approach to directly simulate self-propulsion and turning circle maneuver in waves.

Keywords: self-propulsion; turning circle manoeuvre; wave; RANS; overset

1. Introduction

For the safety of the ship, the verification on the maneuver performance is required. Therefore, the International Marine Organization involves the standard for maneuver in which the minimum requirements for ships from the maneuver point of view are set. In this standard, the criteria such as turning ability, initial turning ability, are course keeping ability are checked in calm water. However, the maneuver performance of a ship on a given route may be significantly affected by the presence of waves. Not only the hull will experience added resistance, mean lateral drift force, and yaw moments in waves, leading to changes in the maneuver path, but also the propulsion characteristic will be influenced by wave-induced ship motion and the orbital wave particle velocities.

To provide a better understanding of maneuver in waves, several experimental tests of maneuver in waves have been performed. Sanada et al. (2013) executed a large series of free running tests of a tumblehome in waves. Zigzag and turning circles tests with different Froude numbers and wave conditions were reported. Sprenger et al. (2016) described the experimental tests conducted in the SHOPERA project. A comprehensive test program of maneuver in waves consisted of more than 1, 300 different model tests for three ship hulls of different geometry and hydrodynamic characteristics, in both deep and shallow water conditions. These experiments provide valuable date to verify the numerical model.

Apart from the free running model tests, computational fluid dynamics (CFD) has become a reliable tool to predict ship maneuver motion. In general, one can predict the maneuver motion by mathematical models or direct numerical simulation. For the mathematical model, CFD can be used to determine the hydrodynamic coefficients. For instance, Cura-Hochbaum and Uharek (2016) used an Abkowitz-type mathematical model to predict the ship's trajectories during turning circles with the calm water hydrodynamic coefficients and the wave-induced forces obtained from virtual captive tests simulated by RANS calculations. After that, Uharek and Cura-Hochbaum (2018) extended this method to

Manuscript received by SNAME headquarters April 4, 2020; accepted May 4, 2020.

Corresponding author: Decheng Wan, dcwan@sjtu.edu.cn

predict the delivered power in the course of maneuver. For direct simulation, Carrica et al. (2013) conducted Unsteady Reynolds-Averaged Navier-Stokes (URANS) simulations for turn and zigzag maneuvers of a surface combatant using dynamic overset grids. Broglia et al. (2016) studied the turning ability for a fully appended twin-screw vessel considering single and twin rudder configuration, respectively. In their studies, overset grids were used to discretize the rudder, whereas the propellers were used in the simplified actuator disk model. Consequently, the predicted results showed reasonable errors with the free running ship tests. Shen et al. (2015) implemented overset grid into OpenFOAM and applied the technique to simulate zigzag maneuver. Wang et al. (2016) further extended the solver in calculating turning circle maneuver with fully discretized propellers and rudders. Then, a series of studies on the maneuverability of Office of Naval Research Tumblehome Ship (ONRT) have been carried out, such as course-keeping simulation (Wang et al. 2017), zigzag maneuver in waves (Wang et al. 2018), and turning circle maneuver in waves (Wang & Wan 2018). Beyond these studies, numerical studies of propulsion characteristics for ships in waves based on solving the Navier–Stokes equations are hardly found in the literature. Recently, Sigmund and el Moctar (2017) conducted propulsion of the freely advancing ships in regular waves. The authors discussed the influence of waves on propeller forces, propeller efficiency, relative rotative efficiency, hull efficiency, thrust deduction, and wake fraction as well as the propulsion efficiency. All the aforementioned research studies proved that the CFD method is a robust and reliable approach to numerically predict ship maneuver performance.

However, previous direct CFD simulations for free running ship maneuver were mostly performed for calm water conditions. In the present work, self-propulsion and turning circle maneuver in waves are conducted using our in-house CFD solver naoe-FOAM-SJTU. This solver includes wave generation and absorption, 6-DOF motion with a hierarchy of bodies, mooring system, dynamic overset grid, fluid-structure interaction has been applied to various applications in marine hydrodynamic problems, such as on ship hydrodynamics, offshore platforms, marine risers, and floating offshore wind turbines (Wang et al. 2019).

The article is framed as follows: first, the open-water characteristic of the propeller is computed. Next, the self-propulsion computation in waves is performed. In the computation, the dynamic overset grid method is adopted to handle the complex motion of the ship hull–propeller–rudder system, while the open-source wave generation tool waves2Foam (Jacobsen et al. 2012) is used to generate desired waves in the moving computational domain. Through this way, direct RANS computations for turning circle maneuver in waves are carried out. After that, the result of the self-propulsion test is used as the initial condition to conduct the turning circle maneuver computation. Because this simulation is time-consuming, the yaw angle only varies from 0 to 90°. After the simulation, the influence of waves on propeller forces, propeller efficiency, and wake fraction is discussed. The effect of waves on propulsion is analyzed by accounting for the phase lag and amplitude decay of water particle velocity caused by the hull. Then the wake fraction is evaluated assuming that a quasi-steady analysis works even in unsteady conditions.

2. Numerical approaches

The incompressible Navier–Stokes equations are the governing equations closed by the *k-ω* Shear Stress Transport (SST) two-equation turbulence model. The wall function is used to resolve the near-wall region. The volume of fluid (VOF) method with artificial compression is used to capture the air/water interface (Berberović et al. 2009). The overset technique is used to handle the large-amplitude motions for a hierarchy of objects in this study. Overset grid is a grid system composed of multiple blocks of overlapping structured or unstructured grids. Boundary information is exchanged between these grids via domain connectivity information produced by Suggar++ (Noack et al. 2009). To implement the wave generation and absorption in the computational domain, the open-source library waves2Foam tool (Jacobsen et al. 2012) is imposed in our solver.

It is practically difficult to impose a suitable wave environment for turning circle simulation. In general, one can impose the wave boundary conditions on the inlet boundary to generate waves and set a damping zone near the outlet to avoid the wave reflection. Such practice may suffer from wave reflections from the inner computational domain to interfere with the wave-maker boundaries, which creates discontinuities in the surface elevation at the wave-maker boundary leading to divergent solutions. The turning circle simulation is more susceptible to such wave reflection because it is a time-consuming case. The reflection wave from the inner domain has enough time to propagate to the wave-maker boundary. It would become worse for beam sea where the wave reflection is more pronounced. Therefore, a tool that allows both wave generation and absorption near the inlet boundary is needed. In the waves2Foam tool, the concept of the relaxation zone is implemented to achieve such requirement. In the relaxation zone (Fig. 1), the variable ϕ, which is either velocity or volume of the fraction for the VOF model, can be expressed as follows:

$$\phi = \alpha_R \phi_{\text{computed}} + (1 - \alpha_R)\phi_{\text{target}}, \tag{1}$$

where ϕ_{target} is the variable as a function of space and time known from Stokes wave theory; ϕ_{computed} is the variable computed from FVM. α_R is used to blend ϕ_{target} and ϕ_{computed} in the relaxation zone. α_R is always 1 at the interface between the inner computational domain and the relaxation zone and is 0 at the inlet boundary. α_R smoothly varies from 1 to 0 in the relaxation zone in an exponential way as follows:

$$\alpha_R = 1 - \frac{\exp\sigma^{3.5} - 1}{\exp 1 - 1}, \tag{2}$$

where $\sigma = 1(\alpha_R = 0)$ at boundary and $\sigma = 0(\alpha_R = 1)$ at the interface between the inner computational domain and the relaxation zone, and σ changes linearly. Such distribution of α_R makes ϕ relaxed

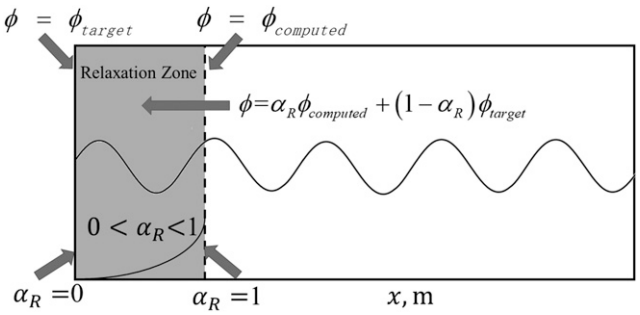

Fig. 1 Sketch of relaxation zone

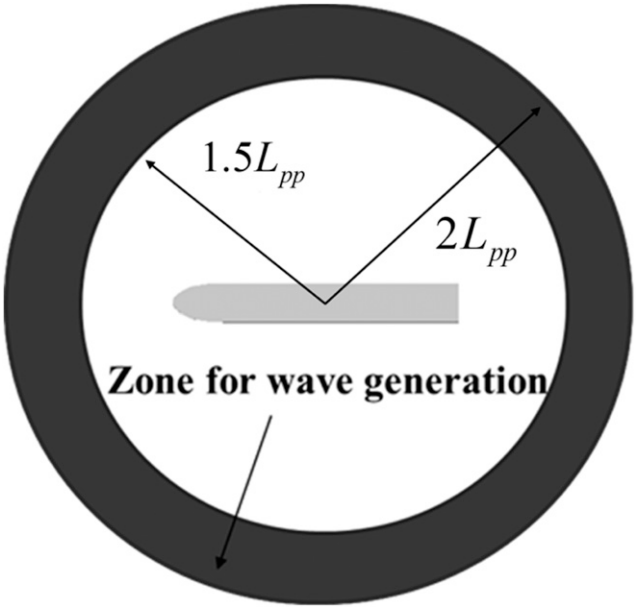

Fig. 2 Top view of the computational domain with the relaxation zone

by the value of $\phi_{computed}$ and ϕ_{target} in the relaxation zone. Through this way, the relaxation zone not only generate waves near the inlet boundary but also absorb the reflection waves, which means it achieves the functionality of both wave generation and absorption in a uniform way.

Figure 2 illustrates the relaxation zone, where a circular ring form zone is used to generate and absorb waves. During the maneuver simulations, the computational domain can move freely in the horizontal plane regarding the ship motion. The relaxation zone is frozen to the computational domain and follow its motion. Therefore, the waves can propagate to the near-ship region regarding the turning circle maneuver.

3. Geometry and grids

3.1. Open-water propeller parameters

The propeller for open-water computation is a fixed-pitch five-bladed propeller with right rotation. This propeller is equipped on Duisburg Test Case (DTC). Table 1 shows its main particulars: the propeller diameter D_P, pitch ratio at .7 of propeller radius $P_{.7}/D_P$, disc ratio A_e/A_0, chord length $c_{.7}$ at .7 of propeller radius, effective skew angle of propeller blades θ_{eff}, and nondimensional hub diameter d_h/D_P. Figure 3 shows it geometric feature.

Table 1 Propeller parameters

		Model scale	Full scale
D_p	m	.14	8.911
$P_{.7}/D_p$	-	.959	.959
A_e/A_0	-	.8	.8
$C_{.7}$	mm	.0504	3.208
ϕ_{eff}	°	31.97	31.97
d_h/D_P	-	.176	.176

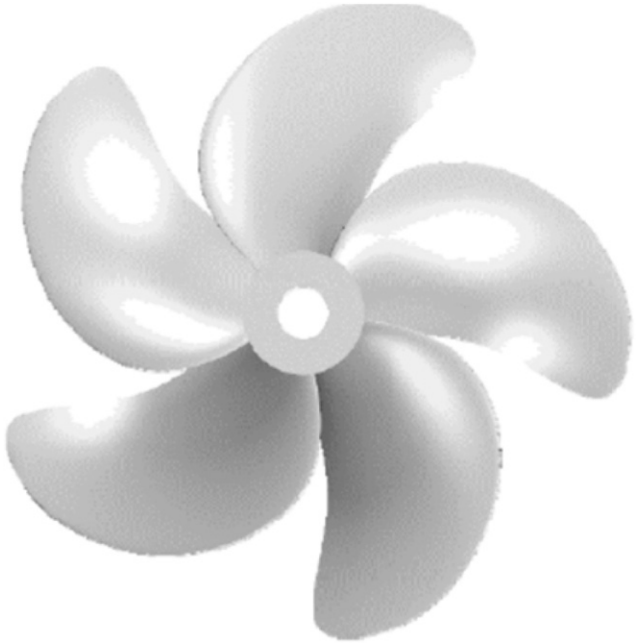

Fig. 3 View of the propeller

For the open-water propeller computation, an earth-fixed frame of reference is used where the propeller is moving with constant rotational speeds and towed with a small acceleration to cover a wide range of advance velocity in a single run. The computations use the single-run procedure described in Xing et al. (2008). The grid system is composed of two parts: overset grid used to follow the rotation of the propeller and background grid used to accommodate the far-field boundary conditions (see Fig. 4). The grids interpolated by Suggar++ are illustrated in Fig. 5. The sizes of these grids are around 3.1 M. Because the wall function is used, the first layer thickness near the wall is set as the average $y+$ is around 30.

3.2. Self-propulsion parameters

The ship model chosen in this study is the DTC container which has comprehensive experimental data from MARINTEK (Trondheim, Norway). The arrangement of model tests can be found in

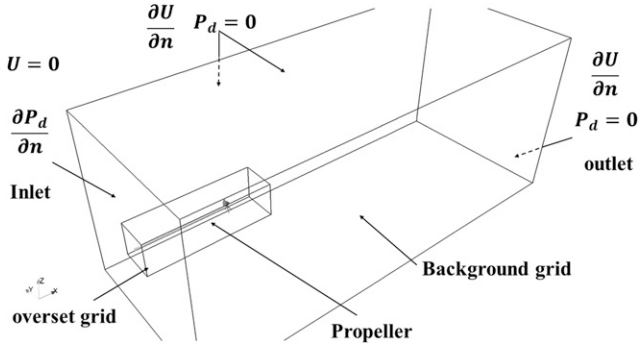

Fig. 4 Design of the overset grid system and boundary conditions for the propeller

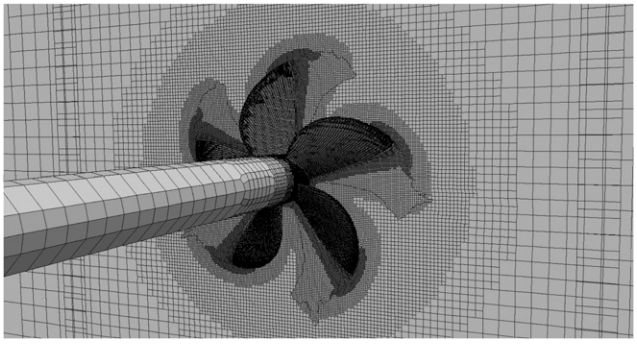

Fig. 5 Overset grids used for open-water computations

Sprenger et al. (2016). The DTC is a generic post-Panamax 14,000 TEU containership developed at the Institute of Ship Technology, Ocean Engineering and Transport Systems of the University of Duisburg-Essen. Its geometry is shown in Fig. 6 appended with a twisted rudder with Costa bulb and an NACA 0018 base profile. The DTC principal particulars are listed in Table 2 in model scale.

On each side of the vessel, a segmented bilge keel is attached symmetrically to the hull along the parallel middle body. But the keels are not considered in this study because the existence of keels increases the complexity of the mesh structure and is harmful to the convergence of computation.

The design of the overset grid system for the DTC is shown in Fig. 7. The cylindrical domain guarantees the proper wave boundary condition during the turning maneuver. The layout of grid system and boundary conditions for self-propulsion calculation is shown in Fig. 8. In this work, the earth system and ship system are used to solve the 6-DOF equation. The motion of the ship is described by translations and rotations with respect to the inertial earth system in terms of the Euler angles, and the linear and angular velocity and the forces and moments are with respect to the ship system. Details of the 6-DOF module can be found in Shen et al. (2015). In computation, the coordinate system is set as follows: the x and y positions of the origin is the same as the center of gravity and the z position of water plane is zero; The longitudinal x axis points fore to aft, the transversal y axis points from the port to the starboard, and the vertical z axis points upward. The background grid can move freely in the horizontal plane regarding the ship motion which is designed to properly capture the free surface.

Local grid distribution around the ship hull, propeller, and rudder is shown in Fig. 9. It should be noticed that artificial gaps between the propeller and the hull, rudder, and rudder root are used to obtain enough interpolation cells. The sizes of these grids are listed in Table 3. For the background grid, 20 points per wave height and 80 grids per wave length are set to avoid wave dissipation. For the hull grid, there are 300 grid points along lengthwise and the bow and stern are further refined to capture wave breaking. For the propulsion, 60 grid points per radius of the propeller and 100 grid

Table 2 Hull parameters

Main particular		Value
Scale factor	λ	1:63.65
Length between perpendiculars	L_{pp}	5.57 m
Molded breadth	B	.80 m
Draft	T	.23 m
Block coefficient	CB	.661
Displacement	Δ	672.7 kg
Wetted hull surface	S_w	5.438 m2
Longitudinal distance of the center of gravity from the aft perpendicular	LCG	2.74 m
Vertical distance of the center of gravity from the base line	VCG	.39 m
Transverse metacentric height	GM_T	.08 m
Gyradius about x axis	r_{xx}	.31 m
Gyradius about y axis	r_{yy}	1.37 m
Gyradius about z axis	r_{zz}	1.37 m

points per average chord length of the rudder are guaranteed. The total grid number for the free running simulations is 8.13 million. The adaptive wall function is used, and the average $y+$ on the wall is around 30. The motion of the grid around the propeller and rudder follows the control laws of specific ship maneuver.

4. Numerical simulations

4.1. Open-water characteristic

The time step is set to $\Delta t = 2 \times 10^{-4}$ seconds for open-water computation. Figure 10 shows that the overset technique predicts the curves quite well and results have a good agreement with experimental data (el Moctar et al. 2012), except for $J > .8$ where η_0 is overestimated. These results indicate that the overset technique is capable of predicting the open-water curves, and the obtained open-water characteristic will be used to estimate the effective wake fraction and thrust efficiency in the condition of self-propulsion.

4.2. Self-propulsion simulation in waves

Before conducting the simulation of waves, present configuration as shown in Fig. 2 should be checked out whether the wave

Fig. 6 View of the DTC hull and the rudder

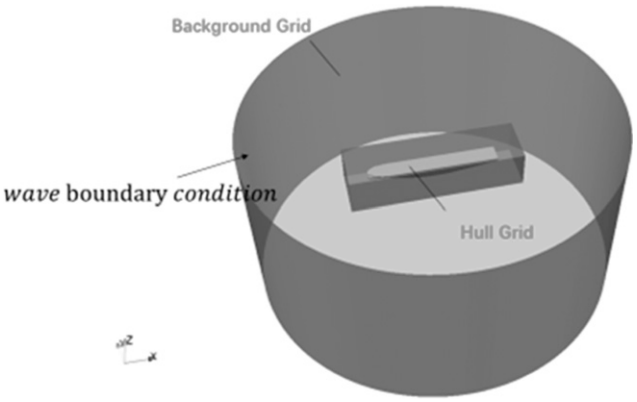

Fig. 7 Design of the overset grid system for DTC

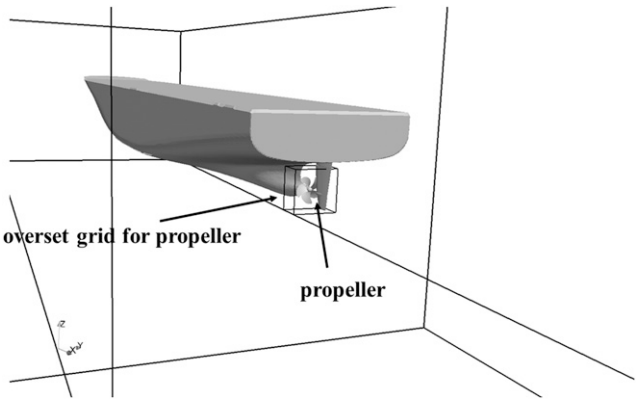

Fig. 8 Overset grid system for self-propulsion calculation

reflection is avoided. The grid used for this validation is the same with the background grid used for the maneuver simulation without hull grids. First-order Stokes wave on deep water with $H = .0628$ m and $T = 1.567$ is generated in the domain. The reflection coefficients C_R can be calculated as follows (Ursell et al. 1960):

$$C_R = (\mathrm{EH}_{\max} - \mathrm{EH}_{\min})/(\mathrm{EH}_{\max} + \mathrm{EH}_{\min}), \tag{3}$$

where $\mathrm{EH}_{\max}$ is the maximum and $\mathrm{EH}_{\min}$ is the minimum value of the wave height envelop as shown in Fig. 11. Figure 11 shows the wave envelope measured on the vertical central plane of the domain along the wave propagation direction. The dashed line indicates the boundary of the relaxation zone. In Fig. 11, some small bumps can be seen on the envelope indicating that the wave reflection is not perfectly diminished in the domain. To estimate the wave reflection, $\mathrm{EH}_{\max}$ and $\mathrm{EH}_{\min}$ are measured as shown the Fig. 11, which are .0643 m and .0628 m, respectively, so that C_R is only 1.2% according to equation (3) and is acceptable. It is noteworthy that this C_R here may be too optimistic. The possible wave reflection from outlet boundary is proportional to the difference between the reference solution (the far-field wave) and the computed flow. In this investigated example, the analytical solution for the incidence waves is not disturbed before traveling into the absorption zone and the difference between the reference wave solution is small. Then the performance of the absorption zone is perfect. Whereas in 3D maneuvering applications, the waves traveling toward the wave

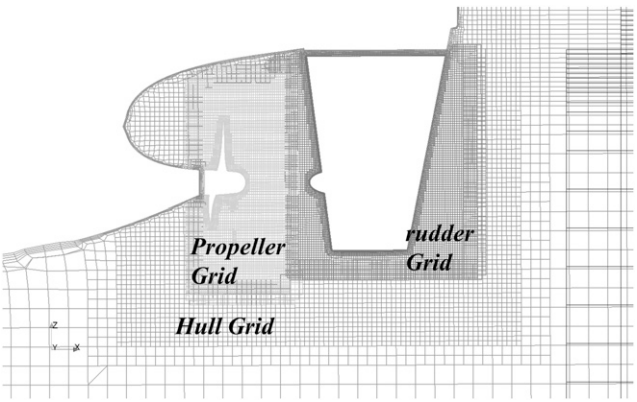

Fig. 9 Overset grid distribution

Table 3 Grid sizes

	Hull	Rudder	Propeller	Background
Cells	1.91M	1.1M	1.22M	3.9M

absorber will be disturbed by the hull, which will differ from the prescribed incidence wave solution. Therefore, the absorption of the reflection wave may be discounted, then reflection may be larger than 1.2% actually.

Then, the simulations of self-propulsion in the wave with $H = .0628$ m and $T = 1.567$ seconds (model scale) are conducted. The first-order Stokes wave theory on deep water is used to generate waves. The model is free to pitch, heave, and surge motions, and the revolutions per second (RPS) of the propeller is set to 6.476 n/sec following the experimental setup (Papanikolaou & el Moctar 2015). According to the experiment, 3° initial rudder angle toward the port side is set to balance the moment caused by the twisted and single screw propeller. The target ship speed is .386 m/sec in the experiment, and the computational ship speed can be used to verify the numerical method. The time step is set to 4×10^{-4} seconds. At each time step, the equation residual is forced to lower than 1e−8, and part of the initial residual during the simulation is showed in Fig. 12. The comparison of ship speed can be seen in Fig. 13. In the computation, the average ship speed is .398 m/sec and is 3% higher than EFD. It gives confidence in our CFD method.

The computational propeller thrust and hull resistance are presented in Fig. 14. The hull resistance shows obvious nonlinearity composing of diffraction and radiation forces. While the thrust is quite linear with small fluctuation induced by nonuniform wake flow.

The pitch and heave motions are shown in Fig. 15. The average pitch motion is around −.3° indicating that the ship oscillates around a bow down position.

The orbital motion of water particle in waves will change the inflow velocity of the propeller. Assuming the linear wave and deep water condition are satisfied, the axial orbital motion velocity near the propeller hub can be described as follows (Ueno et al. 2013):

$$U_{ox} = \alpha\omega \frac{H}{2} \exp(-kz)\cos(kx - \omega t + \varepsilon), \tag{4}$$

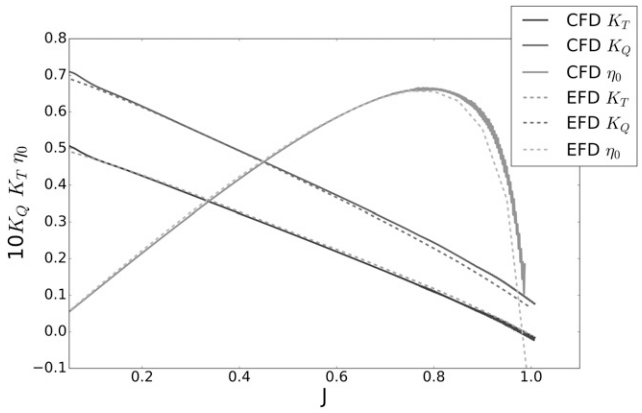

Fig. 10 Open water curves for experiments (dashed lines), single-run (solid lines) procedures

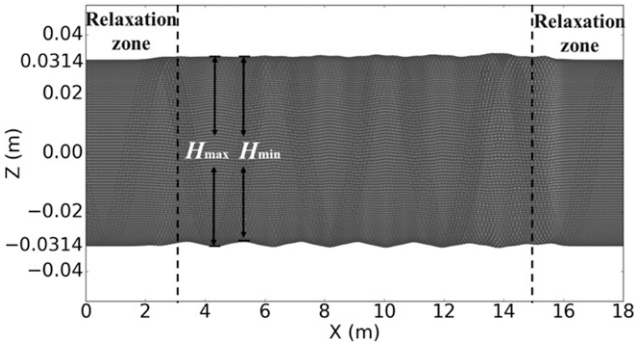

Fig. 11 Wave envelope measured on the vertical central plane

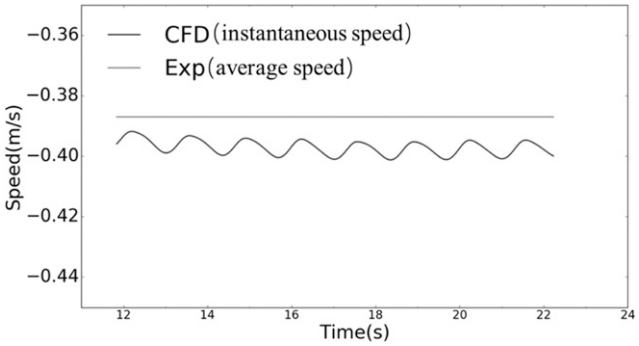

Fig. 13 Comparison of the ship speed between CFD (instantaneous) and EFD (average)

where ω is the wave frequency, k is the wave number, and x and z are the coordinates of the point named as SV on the propeller axis. At the beginning, this point SV is located at $x = 2.564$ m from $L_{pp}/2$ and $z = -.149$ m (the center of the propeller disc is at $x = 2.581$ m from $L_{pp}/2$ and $z = -.149$ m) from the free surface. α represents the effect of the wave amplitude decrease at the stern, and ε represents the phase lag caused by the stern. Note that the encounter frequency is not considered in equation (4) because the x coordinate of SV will change as the ship moves forward and is a variable dependent on time which implicates the encounter frequency. Despite α, the amplitude of the orbital motion velocity at the propeller hub is around 0.1 m/sec. To determine α, the axial flow velocity distribution at the time when the wave crest and trough is at point SV is drawn on the vertical plane as shown in Fig. 16. Here, the plane used to demonstrate the velocity is denoted as SP ($x = 2.581$ m from $L_{pp}/2$). Figure 16 shows that the background axial flow velocity is varied from .06 m/sec to −.075 m/sec because of the orbital motion. On average, α should be .68. Figure 16 shows that the U_{ox} reaches maximum and minimum at 17.07 seconds and 17.8 seconds, respectively. Comparing these two moments with the exact time when the U_{ox} reaches maximum and minimum according to the Stokes wave equation, the phase lag ε should be .4 rad. For now, the effect of orbital motion on axial flow can be roughly estimated. The comparison between U_{ox} estimated by equation (4) and the propeller thrust is shown in Fig. 17. It is obvious that the thrust is 180° out of phase with the orbital motion. The amplitude of axial orbital velocity is 18% of ship speed.

The thrust and torque data in maneuver and open-water characteristics of a propeller in steady calm water provide direct estimation of the advance coefficient, J. This process assumes that a quasi-steady analysis works even in unsteady conditions. Then one can obtain the wake fraction, ω_p, by the following equation:

$$\omega_p = 1 - \left(U_p - U_{ox}\right)/v_{\text{ship}}, \tag{5}$$

where v_{ship} is the instantaneous ship speed and U_p is the inflow velocity obtained by the thrust identification method. Equation (5) eliminates the effect of the orbital motion of water particles on the wake flow.

The effective wake fraction is compared with the vertical motion of the propeller hub as shown in Fig. 18. Figure 18 shows that there is a 180° phase lag between the motion of the propeller hub and the wake fraction. Distinctive oscillations of ω_p are noticeable. It varies from 0 corresponding to the lowest vertical position of the propeller hub to .27 corresponding to the highest vertical position. It suggests that the ship motion changes the inflow velocities by 27% of ship speed. Compared with the axial orbital velocity which is 18% of ship speed, the ship motion has a more obvious effect on the inflow velocity and the propeller thrust.

The ship motion not only changes the wake fraction but also has the influence on the wake flow nonuniformity. Figure 19 shows the instantaneous vertical coordinates of point SV against thrust. It is obvious that the high-frequency fluctuation of thrust is more noticeable at B than A. The axial inflow distribution at A and B

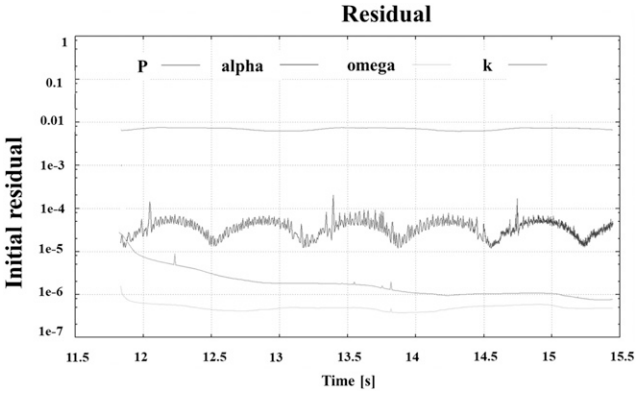

Fig. 12 Initial residual of pressure (p), phase fraction (alpha), turbulence k

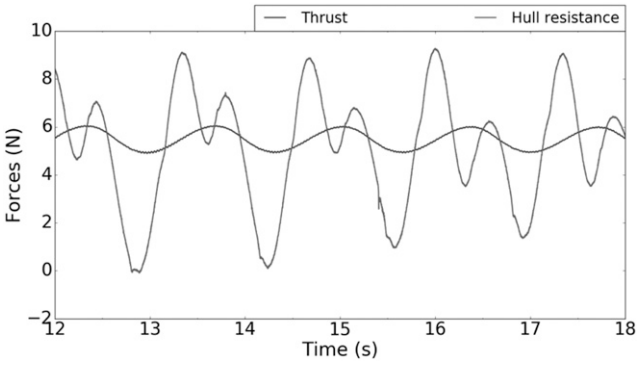

Fig. 14 Time history of hull resistance and thrust during self-propulsion

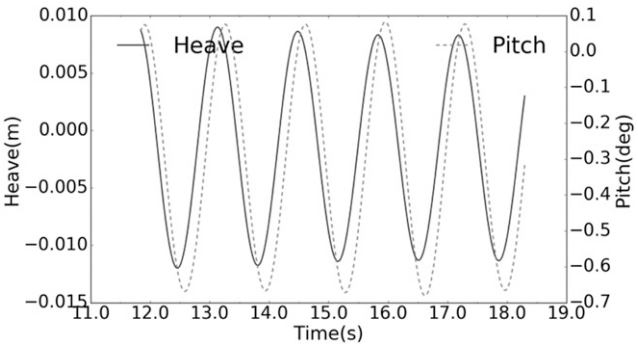

Fig. 15 Heave and pitch motion during self-propulsion computation

moments is shown in Fig. 20. At the A moment, the propeller hub reaches its highest position corresponding to the relatively better wake uniformity as shown in Fig. 20A. When it comes to B, the hub moves downward and reaches its maximum vertical velocity. The wake uniformity at B becomes worse than A corresponding to more pronounced high-frequency fluctuation as shown in Fig. 20. To demonstrate the effect of wake flow on the high-frequency fluctuation, the dynamic pressure distribution on the propeller blade back at A and B is shown in Fig. 21. On the propeller tips, it is obvious that the nonuniformity of the negative pressure region caused by wake flow is more pronounced at B than A.

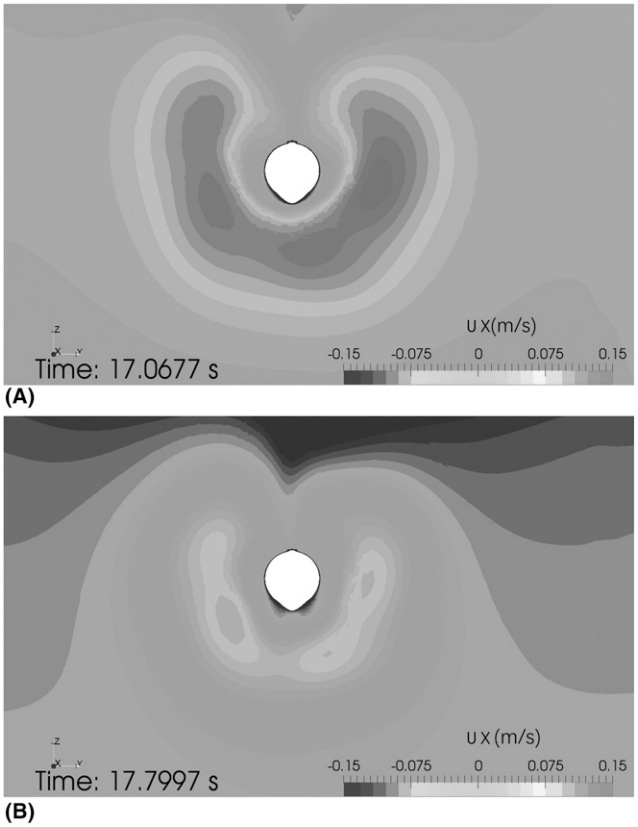

Fig. 16 Axial inflow velocity distribution on the plane SP (perpendicular to the X axis at $x = 2.564$ m from the $L_{pp}/2$): (A) wave crest at the SP, (B) wave trough at the SP

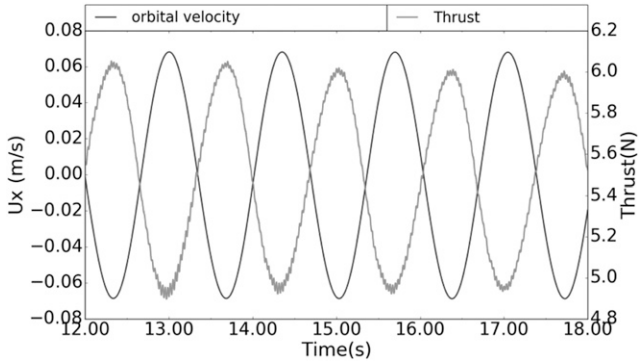

Fig. 17 Orbital motion velocity against propeller thrust

Because the inflow velocity is available, the propeller efficiency can be obtained by the following equation:

$$\eta = U_p \cdot T / 2\pi Q n, \tag{6}$$

where T and Q are the instantaneous thrust and torque of the propeller. The changes of η for self-propulsion computation are shown in Fig. 22.

Figure 22 shows that the oscillation is pronounced as η varies from .32 to .42. The vortical structure around propellers and rudders are depicted in Fig. 23. In this figure, the iso-surfaces of second invariant of the velocity gradient tensor, Q, is used to show the vortical structure. The tip vortices and hub vortices of propellers can be resolved using the present approach. The hub vortices separated from propellers are disturbed by the rudders. While the tip vortices dissipated in front of the rudder, which may be caused by the excessive turbulent viscosity inherent in the RANS model. For the port-side flow, the flow separation at the leading edge of the rudder below the shaft can be observed. This separation is accompanied by the low-pressure region on the rudder. For the starboard side, the separation on the rudder exits above the shaft. These separations are induced by the large attack angle of inflow caused by propeller rotation.

Figure 24 shows the free surface elevation in the computational domain. Because the wave velocity, 2.45 m/sec, is far faster than ship speed, .386 m/sec, the wave pattern before the ship is disturbed. If the boundary condition is used to generate waves, the serious

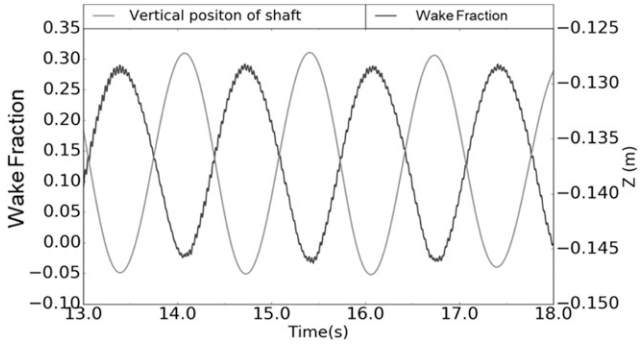

Fig. 18 Effective wake fraction against the vertical motion of the propeller hub

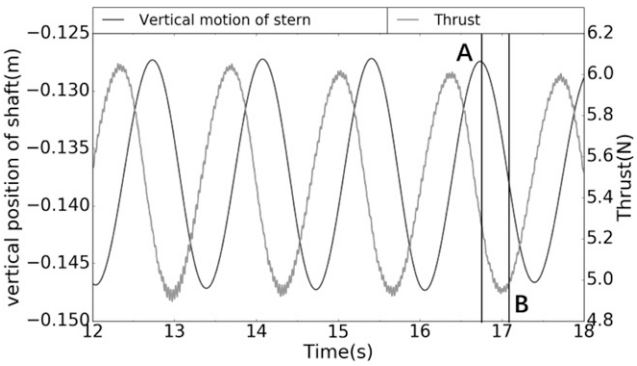

Fig. 19 Vertical coordinate of point SV against thrust

wave reflection from inlet boundary would contaminate the wave pattern around the hull. In this study, the relaxation zone successfully prevents the wave from reflecting in the domain.

4.3. Turning circle maneuver in wave

The wave condition of turning circle maneuver is the same with the self-propulsion test. The rudder angle puts 35° to the starboard when the wave crest is encountered at amidships. The rudder angle

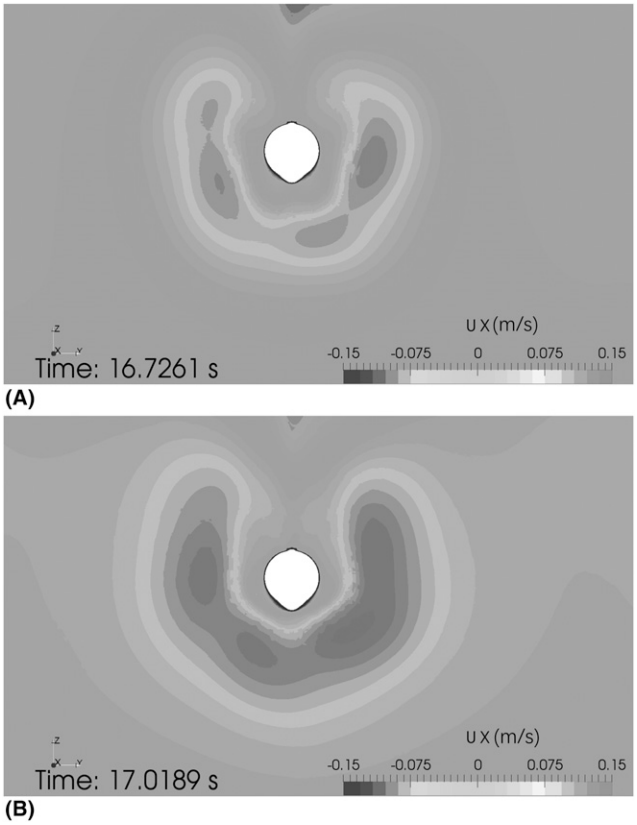

Fig. 20 Axial inflow velocity distribution on plane SP: (A) axial inflow velocity distribution on plane SP at point *A* in Fig. 19, (B) axial inflow velocity distribution on plane SP at point *B* in Fig. 19

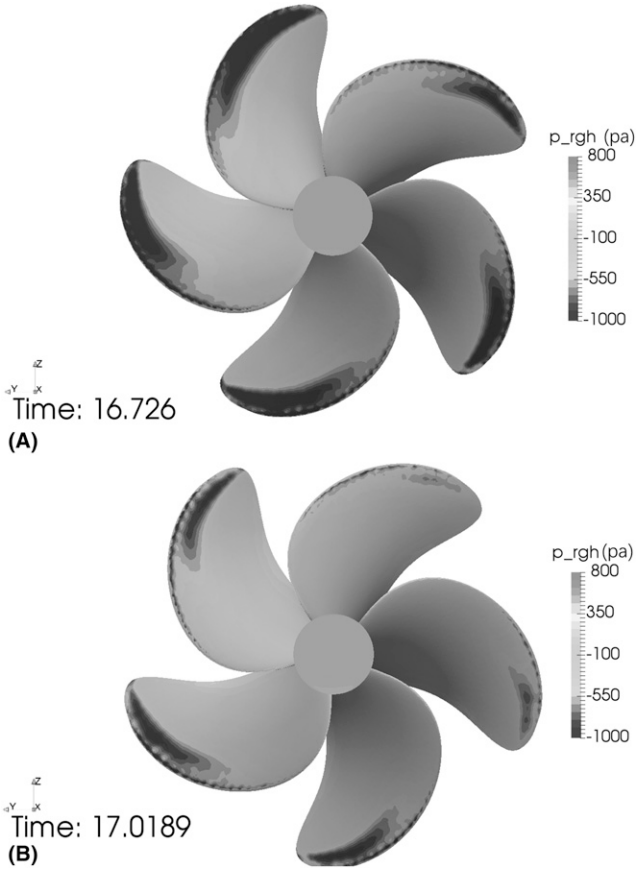

Fig. 21 Dynamic pressure distribution on the blade back: (A) dynamic pressure distribution on the blade back at point *A* in Fig. 19, (B) dynamic pressure distribution on the blade back at point *B* in Fig. 19

rate is 25/sec. The grid system is the same with the self-propulsion computation. The ship speed is .386 m/sec, and propeller speed is 6.476 n/sec. The time step is set to 4×10^{-4} seconds corresponding to 1° propeller rotation per time step. The residual control is the same with self-propulsion case, and its initial residual in each time step is shown in Fig. 25. Because the ship speed is fairly slow, the time consumption of a 360° yaw angle change requires 250-second model scale time simulation. It would take around 200-day wall

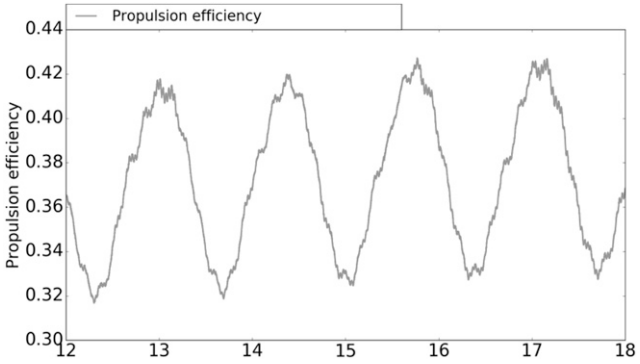

Fig. 22 Propeller efficiency for self-propulsion computation

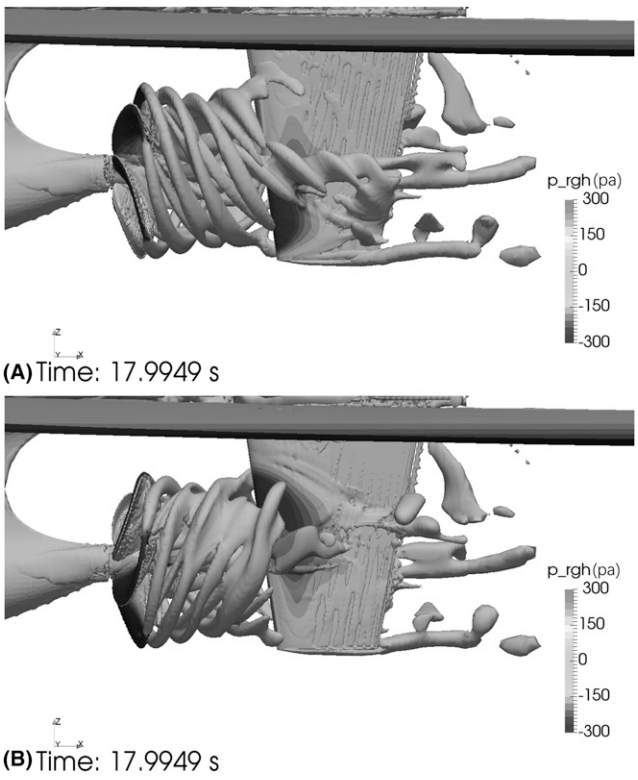

Fig. 23 Isosurfaces of $Q = 200$: (A) port-side view of vortical structures, (B) starboard-side view of vortical structures

clock time with 60 CPU processors. Therefore, only the initial 90° yaw angle turning circle is performed in this study. The initial wave heading is head waves.

Figure 26 shows the predicted yaw motion compared with the rudder angle and trajectory. As the yaw angle increases, the yaw and trajectory curve oscillations induced by the wave become more obvious. The predicted trajectory agreed well with the experiment except for the yaw angle is around 90°.

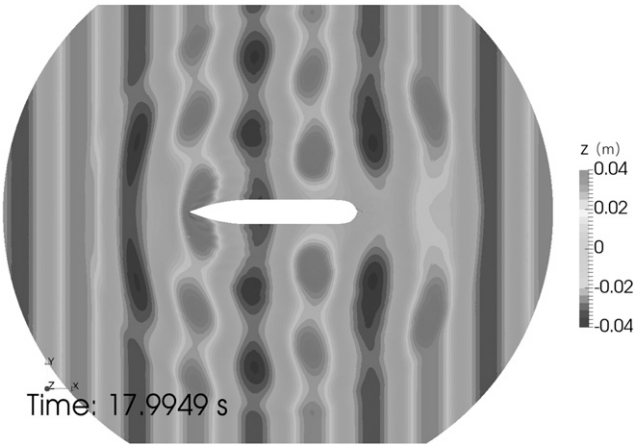

Fig. 24 Free surface elevation

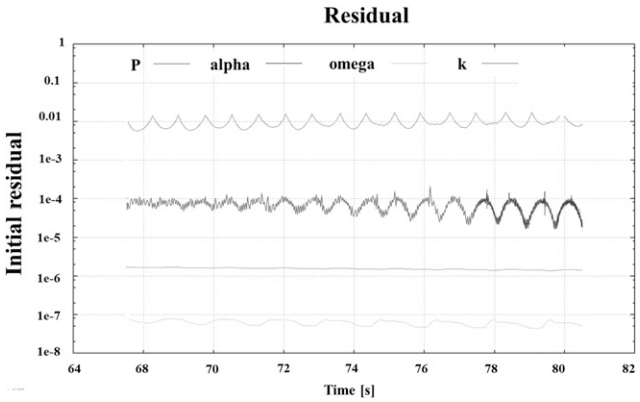

Fig. 25 Initial residual of turning circle case

Figure 27 shows the time histories of instantaneous ship speed and yaw rate during the simulation time. It is clear that the ship speed loss is obvious before the yaw angle reaches 60°. The ship speed drops because of the incident waves and the rudder deflection. When the yaw angle is more than 60°, the average ship speed decreases to .29 m/sec and stops to decrease further. Figure 27B shows that the oscillation of the yaw rate increases as the yaw angle increases and the oscillation caused by the wave becomes more pronounced at the 60° yaw angle.

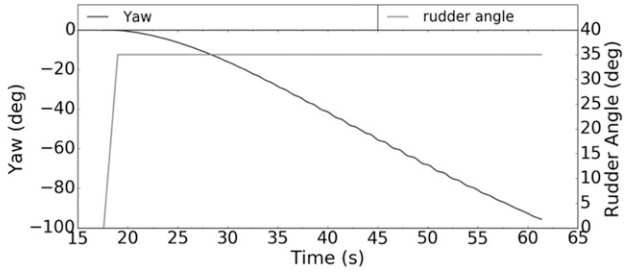

(A) Yaw motion

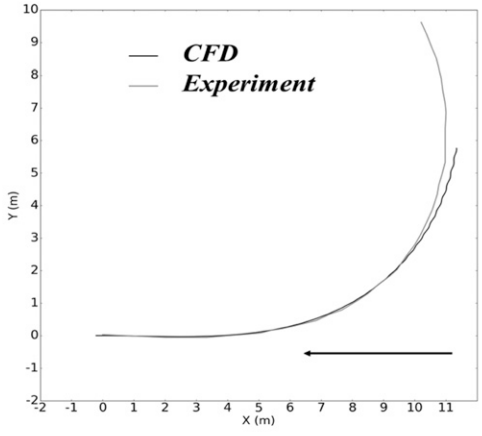

(B) Trajectory

Fig. 26 Yaw angle and trajectory of turning circle maneuver in wave: (A) yaw motion, (B) trajectory

The heave, pitch, and roll motion are shown in Fig. 28. The heave motion begins to increase when the yaw angle is more than 60°. This can be explained as follows:

When the wave length is 3.83 m and the ship length is 5.57 m, their ratio is .687 which means the wave is too short to give rise to the heave motion in head waves, but when the yaw angle is increased, the wave length along the ship length, relevant length, becomes effectively longer in relation to the ship length. The ship's vertical motion begins to follow the motion of the waves. When the yaw angle is 90°, the ship breadth becomes the relevant length which is relatively smaller than wave length. It causes the heave amplitude to be equal to the wave height. For the pitch motion, its oscillation increases as the yaw angle increases and reaches maximum when the yaw angle is around 60°. This is also related to the relevant length. When the wave length is 3.83 m and the ship length is 5.57 m, their ratio is .687 which means the wave is too short to give rise to the pitch motion in head waves. As the yaw angle is more than 60°, this ratio will be equal to 1.2 which will cause the pitch motion effectively.

The time history of thrust and torque of the propeller is shown in Fig. 29. It shows that the torque curve is very similar to the pitch motion indicating that the pitch motion can significantly influence the propulsion efficiency through changing the attack angle of propeller blades. It shows that the thrust is larger during the turning circle than the self-propulsion test and the oscillation becomes more pronounced. As the yaw angle increases, the amplitude of torque oscillation becomes larger because of the roll motion and oblique inflow.

Because the thrust is available, the wake fraction and propulsion efficiency can be analyzed with the assumption that the thrust identification method is effective in oblique waves. To obtain the wake fraction, the effect of orbital motion in waves on axial inflow should be eliminated following equation (4). Taking the encounter angle into account, equation (4) can be extended to oblique waves. Thus, the axial orbital motion velocity is estimated by the following equation:

$$U_{ox} = \cos\psi \cdot \alpha\omega \frac{H}{2} \exp(-kz)\cos(kx - \omega t + \varepsilon), \tag{7}$$

where ψ is the wave heading. At the beginning of the turning circle case, ψ is 0° and then the yaw angle of the ship is used to determine ψ. In the oblique wave, Ueno et al. (2013) assumed the coefficient α as follows:

$$\alpha = \begin{cases} 0.2\left(\dfrac{\lambda}{L_{pp}|\cos\psi|}\right) + 0.5 & \text{for } \dfrac{\lambda}{L_{pp}|\cos\psi|} \le 2.5 \\ 1 & \text{for } \dfrac{\lambda}{L_{pp}|\cos\psi|} > 2.5 \end{cases}. \tag{8}$$

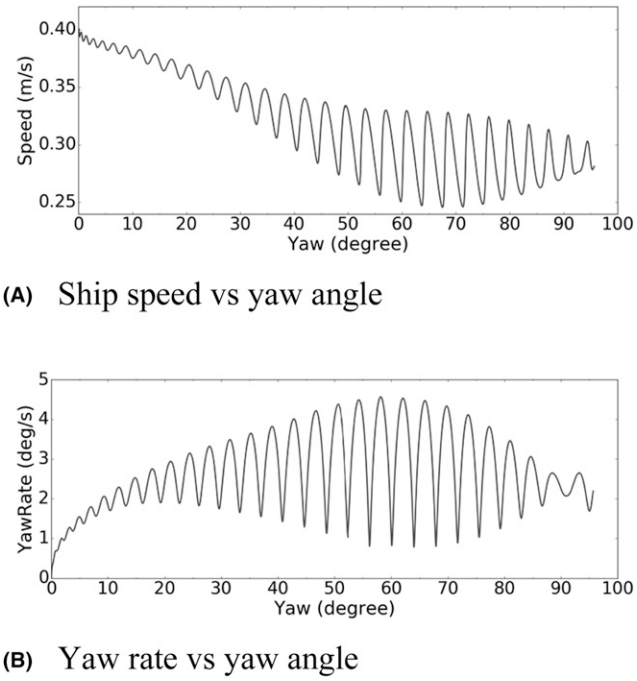

Fig. 27 Ship speed (A) and yaw rate (B) vs yaw angle during turning circle maneuver in wave

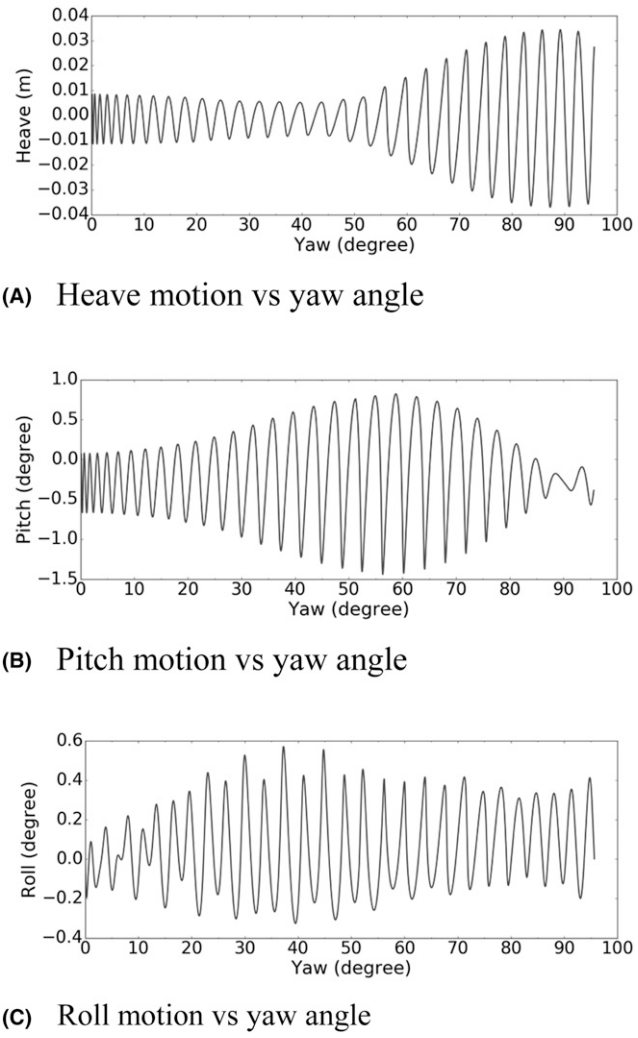

Fig. 28 Heave, (A) pitch, (B) and roll (C) motion vs yaw angle during turning circle maneuver in wave.

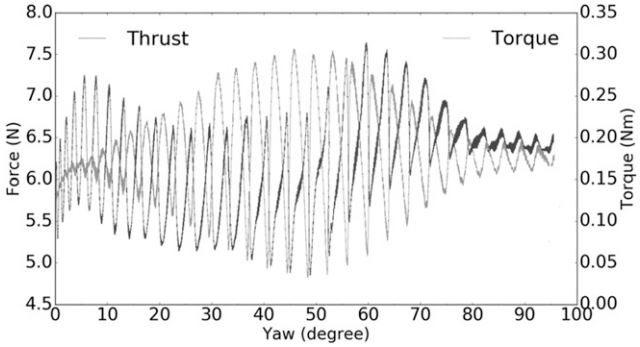

Fig. 29 Thrust and torque vs yaw angle

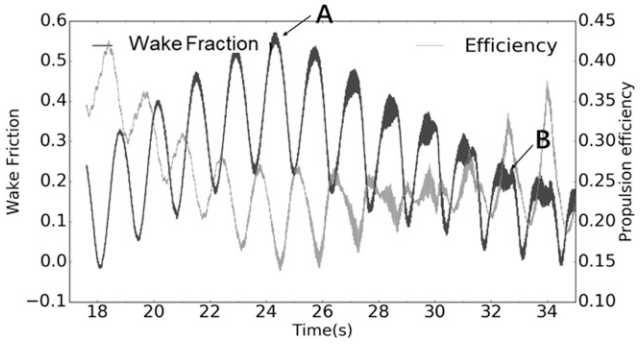

Fig. 31 Wake fraction and propulsion efficiency of turning circle maneuver in waves

Then the phase lag of wave caused by the hull, ε, is assumed as follows:

$$\varepsilon = \varepsilon_0 \cdot \cos\psi, \tag{9}$$

where ε_0 is the phase lag in head waves and should be .4 rad in this case.

Equations (7) and (8) suggest that the phase lag and wave amplitude attenuation at the stern decrease as the ship turns from the head waves to beam waves. In beam waves, the waves directly arrive at the stern instead of first being disturbed by the hull. Therefore, the α should be 1 and ε should be 0 in beam waves. Equations (7) and (8) are intuitively reasonable, but the wave pattern will show strong asymmetry between port and starboard sides of the stern when the encounter angle is large (as shown in Fig. 30). It will lead to the asymmetric orbital motion of water particles around the propeller. Therefore, further validation of equations (7) and (8) is required.

Assuming the thrust identification method works in oblique waves, the wave fraction and propulsion efficiency calculated by equations (5) and (6) are shown in Fig. 31.

Figure 31 shows that the wake fraction first increases to .55 at point *A*, then it decreases to .2 at *B* point. The efficiency has the opposite trend against wake fraction. To give a better description of the wake fraction during the turning circle maneuver, the axial inflow velocity at points *A* and *B* in Fig. 31 is shown in Fig. 32. Its corresponding wave pattern is shown in Fig. 33.

Figure 32 shows that the axial inflow shows asymmetry between port and starboard sides because of the drift angle and yaw motion. The axial inflow velocity at point *A* is smaller than point *B* suggesting that the wake fraction at point *A* is larger than point *B*. The difference of wake fraction between *A* and *B* is caused by the drift angle. Figure 34 shows the time history of the drift angle. As the drift angle increases, the inflow is less disturbed by the hull and

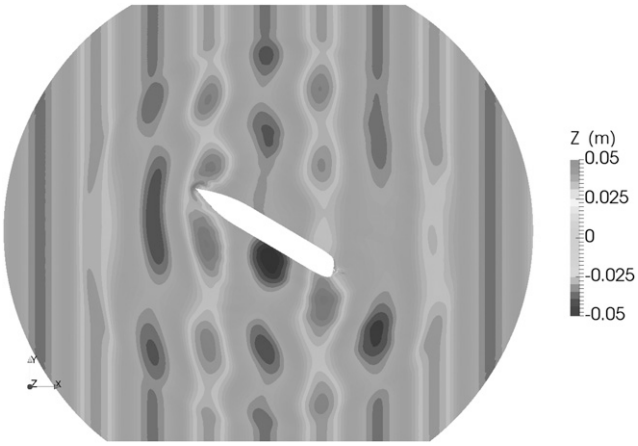

Fig. 30 Free surface elevation when the yaw angle is 30°

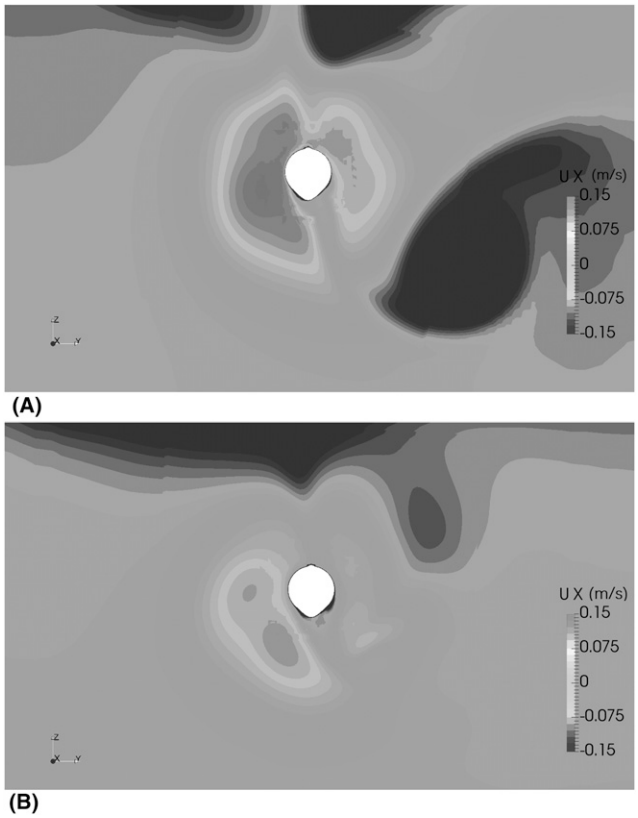

Fig. 32 Axial inflow velocity before the propeller: (A) axial inflow velocity distribution on plane SP at point *A* in Fig. 31, (B) axial inflow velocity distribution on plane SP at point *B* in Fig. 31

directly flows into the propeller. Therefore, the wake effect is weakened at the large drift angle. The axial inflow velocity around the stern distributed on the horizontal cross-section is shown in Fig. 35. Figures 35A and B are corresponding to the point *A* and *B* in Fig. 31. The blue region near the hull is the wake flow. It is obvious that the wake flow at point *A* is more obvious than point *B* because the drift angle at point *A* is relatively small. It is evident that the drift angle has an important influence on the wake flow and further on the propulsion performance.

The vortical structure around propellers and rudders is depicted in Fig. 36. Large flow separation is shown on the port side of rudder due to the attack angle of rudder, which cannot be observed in self-propulsion computation (Fig. 23).

5. Conclusions

In the present work, the self-propulsion and turning circle maneuver in waves are conducted. The ship motion, free surface, and vortex structure are presented. The propulsion performance is mainly analyzed in this study. Assuming the thrust identification method works even in unsteady conditions, the open-water characteristics of a propeller in uniform inflow are used to direct estimates of the inflow velocity and further the wake fraction and propulsion efficiency in maneuver simulation.

The self-propulsion computation in waves is performed with constant propeller rotation speed. The mean advance speed is 3% higher than EFD proving that the present CFD solver is reliable for the self-propulsion test in waves. The time history of thrust shows obvious oscillation. It is induced by the variation of axial inflow which is caused not only by the orbital motion of water particles but also by the ship motion. Then the effect of axial orbital velocity and ship motion is analyzed separately. To estimate the axial orbital motion, the attenuation and phase shift of wave at the stern are considered. Computation shows that the amplitude of axial orbital velocity is 18% of ship

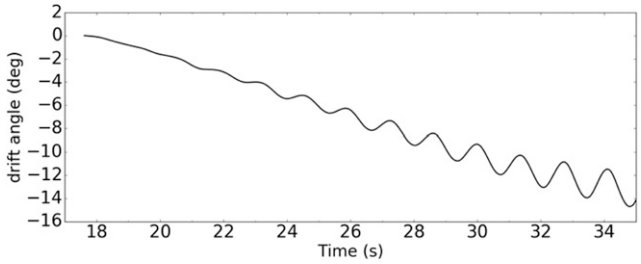

Fig. 34 Time history of drift angle

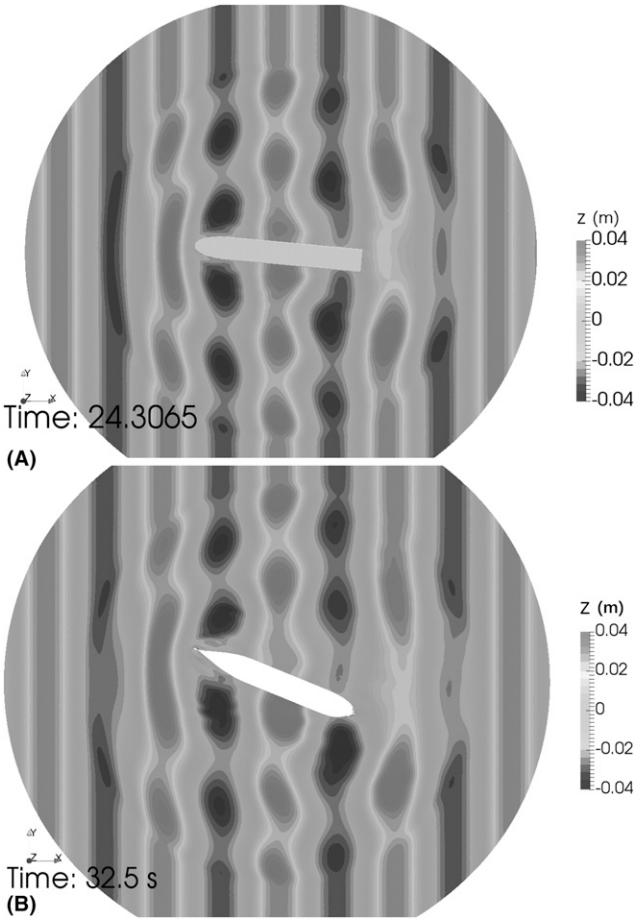

Fig. 33 Free surface elevation during turning circle maneuver in waves: (A) free surface elevation at point *A* in Fig. 31, (B) free surface elevation at point *B* in Fig. 31

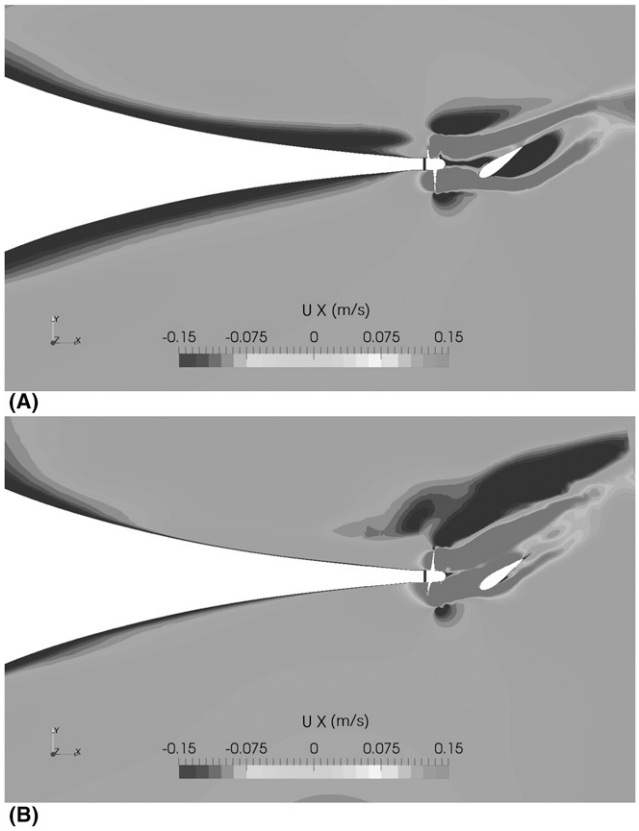

Fig. 35 Axial inflow velocity contours on horizontal cross-sections on the propeller shaft: (A) axial inflow velocity at point *A* in Fig. 31, (B) axial inflow velocity at point *B* in Fig. 31

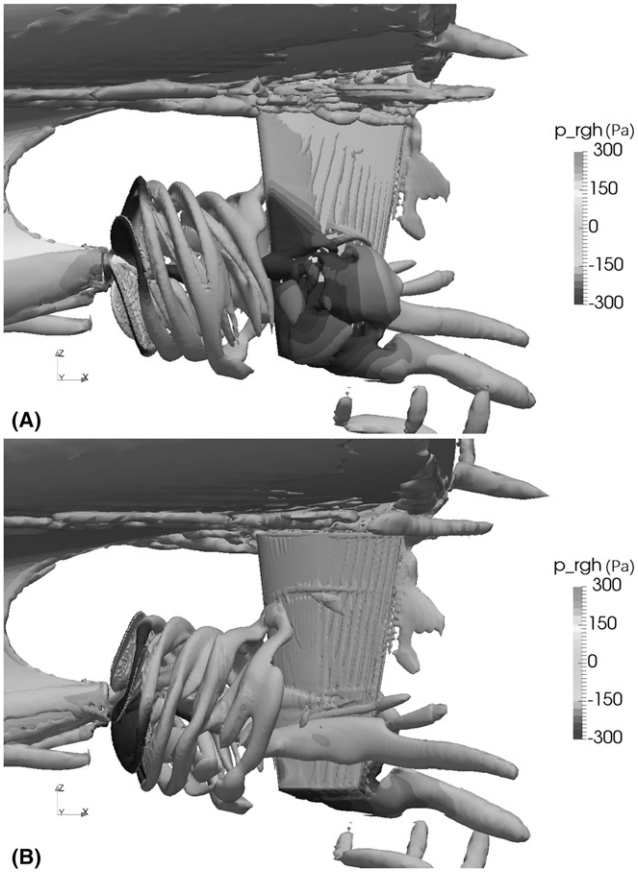

Fig. 36 Isosurfaces of $Q = 200$ when the yaw angle is 30°: (A) port-side view of vortical structures, (B) starboard-side view of vortical structures

speed. After that, the wake fraction is obtained by eliminating the effect of the orbital motion on the wake flow. The oscillation of wake fraction is closely related to the vertical motion of the stern. It suggests that the ship motion can change inflow velocities by 27% of ship speed. In addition, the ship motion can worsen the wake flow and further induce the high-frequency fluctuation of thrust.

After that, the result of self-propulsion computation is used as the initial condition to conduct the turning circle maneuver computation. Because this simulation is time-consuming, the yaw motion only varies from 0 to 90°. The method to estimate the axial orbital velocity is extended to oblique waves. During the turning circle maneuver, the wake fraction is affected by the drift angle. A large drift angle weakens the wake effect of the hull and induces the asymmetric inflow.

In addition, there is still room for further improvement of our results. First, extending our 90° turning circle simulation to 540° will be conducted. Second, some important recent improvements on how to control the relaxation zone to reduce the wave reflection are achieved. We will follow this new technique and move on to the more confident wave absorption technology, such as using the implicit relaxation instead of having a more confident wave reflection expectation (Perić et al. 2018), using the more flexible manner to control which velocity component should be absorbed in the relaxation zone (Perić & Abdel-Maksoud 2019). Finally, how different wave length and steepness cause the change of the wave drift force and further change the trajectory of the ship will be considered in the future.

Acknowledgments

This work is supported by the National Natural Science Foundation of China (51879159 and 51809169), National Key Research and Development Program of China (2019YFB1704200 and 2019YFC0312400), Chang Jiang Scholars Program (T2014099), Shanghai Excellent Academic Leaders Program (17XD1402300), and Innovative Special Project of Numerical Tank of Ministry of Industry and Information Technology of China (September 23, 2016), to which the authors are most grateful.

References

Berberović, E., van Hinsberg, N. P., Jakirlić, S., Roisman, I. V., and Tropea, C. 2009 Drop impact onto a liquid layer of finite thickness: Dynamics of the cavity evolution, *Physical Review E*, **79**, 036306.

Broglia, R., Dubbioso, G., Durante, D., and Mascio, A. D. 2016 Turning ability analysis of a fully appended twin screw vessel by CFD. Part I: Single rudder configuration, *Ocean Engineering*, **117**, 259–271.

Carrica, P. M., Ismail, F., Hyman, M., Bhushan, S., and Stern, F. 2013 Turn and zigzag maneuvers of a surface combatant using a URANS approach with dynamic overset grids, *Journal of Marine Science and Technology*, **18**, 166–181.

Cura-Hochbaum, A. and Uharek, S. 2016 Prediction of ship manoeuvrability in waves based on RANS simulations, *Proceedings*, 31st Symposium on Naval Hydrodynamics, September 11–16, Monterey, CA.

el Moctar, O., Shigunov, V., and Zorn, T. 2012 Duisburg test case: Post-panamax container ship for benchmarking, *Ship Technology Research*, **59**, 50–64.

Jacobsen, N. G., Fuhrman, D. R., and Fredsøe, J. 2012 A wave generation toolbox for the open-source CFD library: OpenFoam®, *International Journal for Numerical Methods in Fluids*, **70**, 1073–1088.

Noack, R. W., Boger, D. A., Kunz, R. F., and Carrica, P. M. 2009 Suggar++: An improved general overset grid assembly capability, *Proceedings*, 19th AIAA Computational Fluid Dynamics, June 22–25, San Antonio, TX.

Papanikolaou, A. and el Moctar, O. 2015 SHOPERA Benchmark Specification Part I: The DTC Case Study, http://shopera.org/benchmark-study/.

Perić, R. and Abdel-Maksoud, M. 2019 Reducing undesired wave reflection at domain boundaries in 3D finite volume–based flow simulations via forcing zones, *Journal of Ship Research*, **64**(1), 23–47.

Perić, R., Vukčević, V., Abdel-Maksoud, M., and Jasak, H. 2018 Tuning the case-dependent parameters of relaxation zones for flow simulations with strongly reflecting bodies in free-surface waves, ArXiv180610995 Phys.

Sanada, Y., Tanimoto, K., Takagi, K., Gui, L., Toda, Y., and Stern, F. 2013 Trajectories for ONR tumblehome maneuvreing in calm water and waves, *Ocean Engineering*, **72**, 45–65.

Shen, Z., Wan, D. C., and Carrica, P. M. 2015 Dynamic overset grids in OpenFOAM with application to KCS self-propulsion and maneuvreing, *Ocean Engineering*, **108**, 287–306.

Sigmund, S. and el Moctar, O. 2017 Numerical and experimental investigation of propulsion in waves, *Ocean Engineering*, **144**, 35–49.

Sprenger, F., Hassani, V., Maron, A., Delefortrie, G., Van Zwijnsvoorde, T., Cura-Hochbaum, A., and Lengwinat, A. 2016 Establishment of a validation and benchmark database for the assessment of ship operation in adverse conditions, *Proceedings*, 35th OMAE V001T01A039, June 19–24, Busan, South Korea.

Ueno, M., Tsukada, Y., and Tanizawa, K. 2013 Estimation and prediction of effective inflow velocity to propeller in waves, *Journal of Marine Science and Technology*, **18**, 339–348.

Uharek, S. and Cura-Hochbaum, A. 2018 Power Prediction for Safe Manoeuvring in Waves, *Proceedings*, 32nd Symposium on Naval Hydrodynamics, August 5–10, Hamburg, Germany, p. 12.

Ursell, F., Dean, R. G., and Yu, Y. S. 1960 Forced small-amplitude water waves: A comparison of theory and experiment, *Journal of Fluid Mechanics*, **7**, 33–52.

Wang, J. and Wan, D. C. 2018 CFD investigations of ship maneuvreing in waves using naoe-FOAM-SJTU solver, *Journal of Marine Science and Application*, **17**, 443–458.

Wang, J., Zhao, W., and Wan, D. C. 2016 Free maneuvreing simulation of ONR tumblehome using overset grid method in naoe FOAM SJTU [C], *Proceedings*, 31st Symposium on Naval Hydrodynamics, September 11–16, Monterey, CA.

Wang, J., Zhao, W., and Wan, D. C. 2019 Development of naoe-FOAM-SJTU solver based on OpenFOAM for marine hydrodynamics, *Journal of Hydrodynamics*, **31**(1), 1–20.

Wang, J., Zou, L., and Wan, D. C. 2017 CFD simulations of free running ship under course keeping control, *Ocean Engineering*, **141**, 450–464.

Wang, J., Zou, L., and Wan, D. C. 2018 Numerical simulations of zigzag manouvre of free running ship in waves by RANS-overset grid method, *Ocean Engineering*, **162**, 55–79.

Xing, T., Carrica, P., and Stern, F. 2008 Computational towing tank procedures for single run curves of resistance and propulsion, *Journal of Fluids Engineering*, **130**, 101102.